

Thermo-mechanical analysis of liquid rocket engine regenerative cooling system: a comparison of hardening models.

*Original*

Thermo-mechanical analysis of liquid rocket engine regenerative cooling system: a comparison of hardening models / Sesana, R., Delprete, C., Pizzarelli, M.. - (2024). (75th International Astronautical Congress (IAC) Milan, Italy 14-18 October 2024.).

*Availability:*

This version is available at: 11583/2996645 since: 2025-01-16T20:26:02Z

*Publisher:*

75th International Astronautical Congress (IAC) Proceedings

*Published*

DOI:

*Terms of use:*

This article is made available under terms and conditions as specified in the corresponding bibliographic description in the repository

*Publisher copyright*

(Article begins on next page)

## Thermo-mechanical analysis of liquid rocket engine regenerative cooling system: a comparison of hardening models.

Matteo Crachi<sup>a\*</sup>, Marco Pizzarelli<sup>b</sup>, Raffaella Sesana<sup>a</sup>, Cristiana Delprete<sup>a</sup>

<sup>a</sup> *Department of Mechanical and aerospace engendering (DIMEAS), Politecnico di Torino University, Corso Duca degli Abruzzi 24, 10129, Turin (TO), Italy*

<sup>b</sup> *Agenzia Spaziale Italiana (ASI), Via del Politecnico, 00133, Rome (RM), Italy*

\* Corresponding Author

**Keywords:** Liquid rocket engine, Low cycle fatigue, hardening models, life prediction.

### Nomenclature

### Acronyms/Abbreviations

NASA Lewis Research Center (LeRC), Liquid Rocket Engine (LRE), Regenerative Cooling System (RCS), Yield Strength (YS)

## 1. Introduction

The thrust chamber of high-performance bipropellant liquid rocket engines is a critical component of reusable launch vehicles. The regenerative cooling system is designed to reduce the temperature of the chamber walls exposed to hot gases and increase the energy of the fuel or oxidizer before injection. In order to guarantee the integrity of the thrust chamber and the reusability of the hardware, thermo-mechanical life prediction is crucial.

Due to low-cycle thermal fatigue during multiple hot firings, the life of regeneratively cooled thrust chambers is directly correlated with their thermal behaviour. Therefore, it is of primary importance to implement validated thermal models into the design process. The requirement of reducing the temperature of the walls exposed to hot gases can be met with high-thermal conductivity copper alloys, while the mechanical stiffness of the external jacket is often achieved by using high-strength steel or nickel alloys. The difference in materials and thicknesses between the internal and external walls can be identified as the major source of severe strains, leading to multiple challenges in the design of regeneratively cooled thrust chambers.

It is known that life estimation of this particular hardware suffers from overestimation due to a lack of reliable representative simplified specimen characterization. Hence, even today, multiple hot-fire tests of a thrust chamber are the only reliable method of assessing its life. However, this approach is time-consuming and expensive. Therefore, despite the great uncertainties about the characterization of materials

under such severe and peculiar operating conditions, numerical thermomechanical simulations are often used to estimate the operating life of these devices.

To try to understand the effect of the numerical models on the life estimation, this study is aimed to explore, using a commercial structural finite element method solver, various hardening models to predict the stress-strain behaviour of a regeneratively cooled thrust chamber.

## 2. Material and methods

### 2.1 SN40 NASA Lewis Research Center

During the Spece Shuttle Main Engine program, LeRC was involved in an experimental test campaign with the aim of studying the low-cycle thermal fatigue of subscale representative model of the SSME [1].

The subscale thrust chambers, so called ‘plug-chambers’, were designed with the purpose to master the life time, the wall temperature vs time distribution, and the mechanical behaviour of RCS failure mechanism. The ultimate goal was to explore copper-based alloys for the inner walls of the hot gas side of the SSME. Amzirc, Narloy-z and OFHC copper were explored as a possible candidate for the gas side inner milled layer, while the electroformed copper was employed for closing out the backside.

The plug-chambers assembly were composed of an injector head element, a water cooled central plug, responsible to generate the axisymmetric convergent-divergent profile, and a cylindrical thrust chamber (Fig. 1).

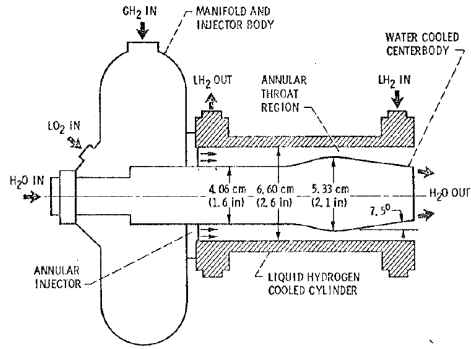
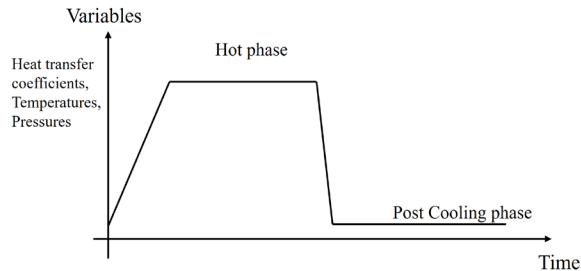


Figure 1. - Schematic of cylindrical thrust chamber assembly.

**Fig. 1 – Plug chamber assembly. Image taken from [1].**

In the present study, the results of the test article SN40 is utilised as the reference case due to the availability of cycling material characterization [1] and temperature distribution data [2]. In particular, SN40 is characterised by an electroformed close out copper layer and a Amzirc milled inner liner (Fig. 3).

All tests have been conducted to ensure multiple identical subsequential cycles until the cylindrical chamber inner wall fails. Liquid hydrogen is continuously circulated in the RCS cooling circuit, ensuring the target wall temperature between cycles. The single cycle has a duration of 3.5 s, 1.7 s from ignition to steady state and 1.8 s of post cooling. The nominal pressure of the chamber is 40 bar [1]. The typical single cycle is reported in Fig. 2.



**Fig. 2 – Typical single LeRC Plug chambers typical cycle history.**

In order to monitor the temperature distribution during cycles, the cylindrical section is equipped with thermocouples at different locations in the throat section. In fact, the throat section, being the most thermally stressed, is the first to fail. Fig. 3 shows the throat cross section, where two ribs of the seventy-two constant area channels are equipped with a thermocouple. One thermocouple is located at a radial distance of 0.89 mm from the hot gas interface, which correspond to the inner wall thickness. The second thermocouple is located at 1.78 mm from the hot gasses, which correspond to the mid radial distance of the ribs.

The SN40 plug-chamber geometry, together with the RCS dimensions, is reported in Fig. 3.

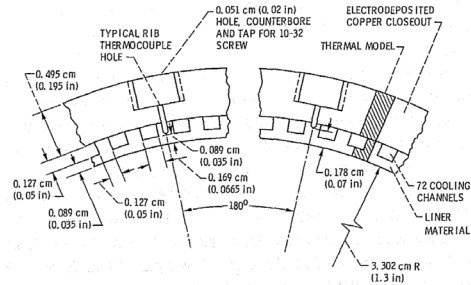


**Fig. 3 – Cross section of the cylindrical chamber. Image taken from [1].**

## 2.2 Finite Element Method setup

The thermo-structural analysis is performed with respect to the throat section of the SN40 LeRC plug chamber.

The computation consists in two different main steps. First, the transient thermal analysis of the geometry is computed with respect to the nominal single chamber cycle. Next, the thermal solution of the first cycle is used as a boundary condition for the static mechanical analysis that is performed in the multiple and sequential time instants. In this study, a total of 40 cycles have been simulated. Note that the first mechanical cycle is computed with an initial wall temperature equal to room temperature. This initial condition is imposed in order to replicate the real experiment setup and, consequently, to take into account its effect on the mechanical behaviour of the first and consequent cycles.

The modulation of the considered thermal and mechanical loads of a single cycle, to be used as boundary conditions of the computations, are represented in Fig. 4. The RCS thermal boundary conditions are represented by a forced convection heat transfer coefficient and reference temperature over the wall interfaces with the coolant and the hot gas. Note that the heat transfer coefficient is different for each side of the rectangular channel (bottom, lateral and top), even if a constant value is considered on each side. On the other hand, a constant reference temperature, equal to the coolant bulk temperature, is imposed on the 3 sides of the rectangular channel. Similarly, the hot-gas side wall convective heat transfer is taken into account by imposing a heat transfer coefficient and a reference temperature. The hot gas side heat transfer coefficient and reference temperature at steady state thrust are taken from the values reported in literature, also with the support of experimental measurements, for the considered test article. Note that the reference temperature is the adiabatic wall temperature. Finally,

the interface with the external environment is considered adiabatic. Although a certain heat transfer to the external environment through the closeout is present in the real case, this heat transfer can be considered negligible in the inner parts of the structure.

The magnitude of the imposed mechanical and thermal boundary conditions varies with time as shown in Fig. 4, that is, by means of a linear segments that range from 0 – corresponding to a chamber-off condition – to 1 – corresponding to a chamber-on condition. Note that the value (0) of the function shown in Fig. 4 does not represent the absolute magnitude of the variables, but rather the condition when the thrust chamber is off. All boundary conditions are listed in Table 1, according to the time phases of the cycle presented in Fig. 4.

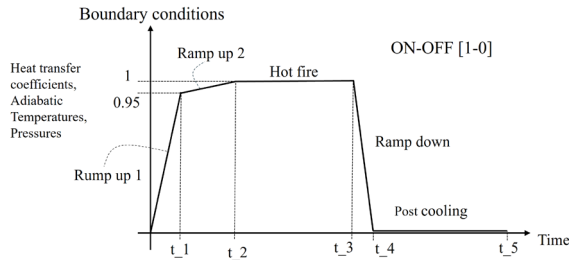


**Fig. 4 – Numerical nominal cycle**

The non-structured computational grid is composed by a total of 903 linear (one integrational point) quadrilateral solid elements and 1990 nodes. The average elements dimensions is forced to be 0.1 mm, comparable with the  $z$  depth dimension, which is assumed according with the main axisymmetric axis of the thrust chamber. The structural analysis considers non-linear effects and large deformations. Both materials (Amzirc and electroformed copper) are modelled as non-linear with temperature dependent properties.

To allow expansion and contraction of the thrust chamber in radial direction ( $r$ -direction in Fig. 5), it is constrained by means of rotational symmetry at the two  $r$ - $z$ -symmetry-planes of the half chamber segments. The displacement of the top surface is fixed in thickness direction ( $u_z = 0$ ), while the opposite side surface nodes are coupled together in the  $z$ -direction.

The coupling is needed to guarantee the generalised plain strain condition, allowing the  $z$ -displacements of one of the two  $r$ - $c$  planes (Fig. 5) to be parallel to the opposite plane. This mechanical condition has been found [3] to be more representative, with respect to the plain strain condition, of the real cycling behaviour of regenerative cooled thrust chamber by reducing the over strain prediction of the 3D analysis and the under prediction of the 2D common plain strain numerical setup [3].

**Table 1 – Numerical nominal cycle external loads.**

Variables	Unit	Ramp up 1	Ramp up 2	Hot fire	Ramp down	Post cooling
$\Delta t$	[s]	0.25	0.85	1.7	2.2	3.5
$p_c$	[bar]	62.2	51	65.5	51	51
$p_{hg}$	[bar]	26.1	27.5	27.5	1	1
$p_{out}$	[bar]	1	1	1	1	1
$h_{hg}$	[kW/m <sup>2</sup> /K]	19	20	20	0	0
$T_{hg}$	[k]	3125.5	3290	3290	294	294
$h_{c\_top}$	[kW/m <sup>2</sup> /K]	152	160	160	150	150
$h_{c\_lateral}$	[kW/m <sup>2</sup> /K]	32.3	34	34	75	75
$h_{c\_botom}$	[kW/m <sup>2</sup> /K]	32.3	34	34	75	75
$T_c$	[k]	54.1	57	57	29	29

While the mechanical and the hot-gas side thermal boundary conditions are taken from the values derived from the experimental activity and reported in the literature, the coolant thermal boundary condition have been iteratively found to match the numerical results with the time-dependent temperature measures taken with the immersed thermocouples (Fig. 6).

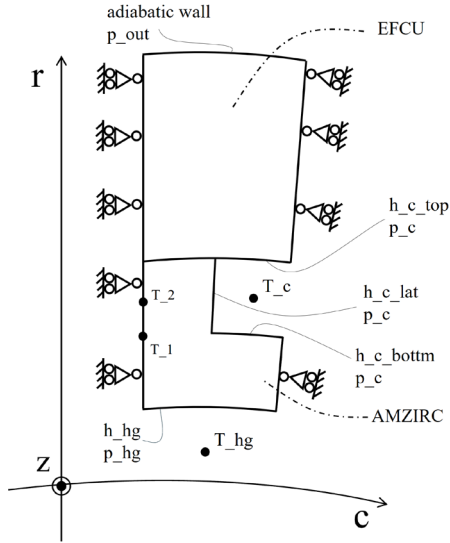


**Fig. 5 – Mechanical and thermal boundary conditions scheme.**

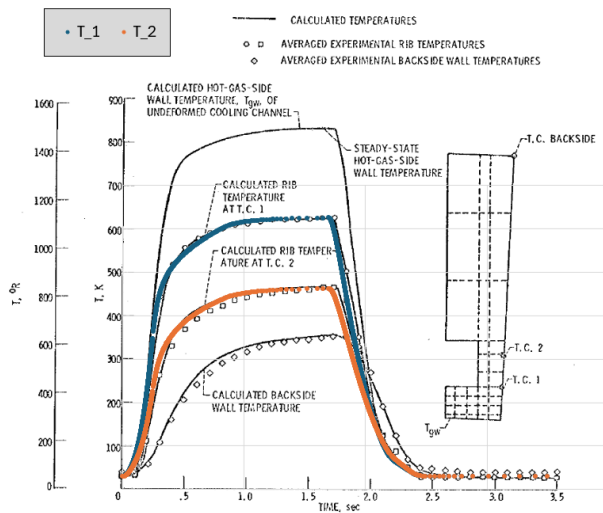


**Fig. 6 – Experimental versus numerical wall temperature time variation of SN40 [1].**

### 3. Theory and calculation

Physical and mechanical properties of Amzirc and electroformed copper are implemented as temperature dependent considering the NASA characterization presented in [2]. Moreover, the data of monotonic-tensile and cyclic mechanical tests of Ref. [2] are used to calibrate the isotropic, kinematic, Chaboche hardening models.

#### 3.1 Multilinear isotropic and multilinear kinematic hardening models

The isotropic hardening is a plastic model able to replicate the hardening and softening behaviour of a structure, but not the Bauschinger effect. The variability of the stresses or strain over the cycles is taken into account by considering a dependency of the yield strength, in the yield function, from the accumulated plastic strain. On the other hand, kinematic hardening material models assume translation of the loading surface as a rigid body in the stress space simultaneously maintaining size, shape and orientation of the initial yield surface. This model is able to replicate the Bauschinger effect.

In the present study both, multilinear isotropic and kinematic models are implemented for both Amzirc and electroformed copper with temperature dependency. Considering the monotonic tensile stress-strain curves available for both materials in [2], the plastic strains versus plastic stresses curves are implemented in tabular format (Fig. 7 and Fig. 8) together with the yield strength and the Young modulus (Table 2).

**Table 2 – AMZIRC and electroformed copper (EFCU) temperature dependent mechanical properties.**

Temperature [K]	E [GPa]	YS [MPa]	E [GPa]	YS [MPa]
	EFCU		AMZIRC	
27,6	118	78	130	293
294,3	114	51	115	209
533,1	109	40	103	131
755,4	105	30	85	59

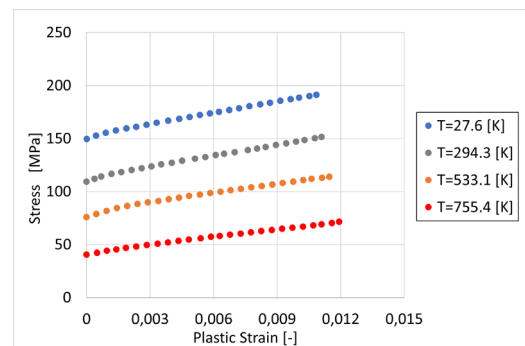


**Fig. 7 – Monotonic back stress - plastic strain curves of electroformed copper extracted from experiments of [2].**

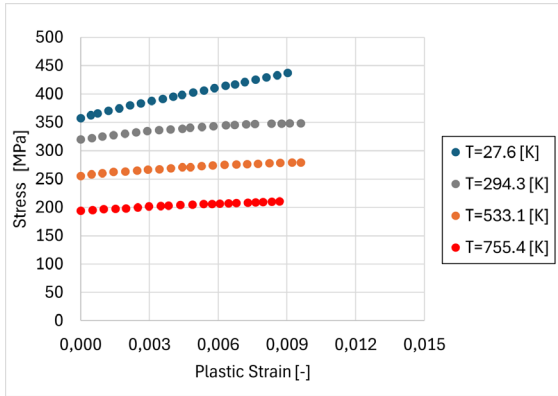


**Fig. 8 – Monotonic back stress - plastic strain curves of Amzirc extracted from experiments in [2].**

### 3.2 2<sup>nd</sup> Chaboche hardening model

In order to calibrate the 2<sup>nd</sup> order Chaboche coefficients, data of cyclic mechanical tests at different total strain amplitude and temperatures are needed. However, electroformed copper cyclic curves are not available in [2]. Hence, for this material the 2<sup>nd</sup> order Chaboche coefficients have been calibrated by considering the back stresses monotonic tensile curves available at 27.6 K, 294.3 K, 533.1 K and 755.4 K. The electroformed coefficients are calibrated considering as the yield strength the first stress when the plastic strains switch from negative to positive (see Fig. 9), and not with the standard 0.2% rules proposed by ASTM E8. This approach has been found to be more accurate in predicting the material Chaboche 2<sup>nd</sup> order coefficients [4]. Note that the stress-plastic strain monotonic curves should be composed by a vertical line before yielding. This is not the case, as visualised in Fig. 9 because of possible experimental set-up errors [5].

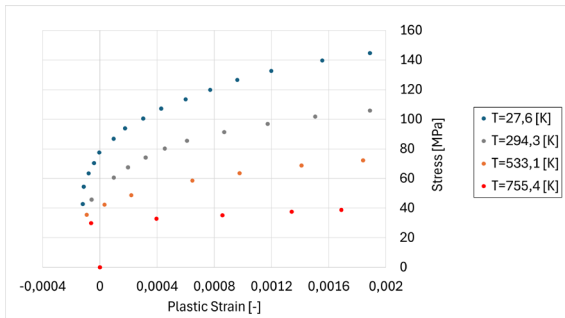


**Fig. 9 – Monotonic tensile stress – plastic strain of electroformed copper curves.**

The coefficients found for the electroformed copper are given in Table 3. Note that, comparing the analytical computation with respect to the experimental curve, it is possible to compute the R.M.S. error.

**Table 3 – 2<sup>nd</sup> order electroformed copper Chaboche coefficients.**

Coefficients	27.6 [K]	294.3 [K]	533.1 [K]	755.4 [K]
EFCU				
RMS error	0.10	0.13	0.09	0.02
C1	80.2	82.6	31.9	4.1
$\gamma_1$	1188	1697	1065	435.1
C2	3.3	4.7	4	2.1
$\gamma_2$	3.1	43.7	43.2	- 2.1

The experimental Amzirc cyclic curves are available only at 294.3 K and 810.9 K [2] and at a single strain range magnitude equal to 2%. Therefore, the 2<sup>nd</sup> order Chaboche coefficients at these temperatures are found using the back stress – plastic strain curves derived with the available cyclic curves. At cryogenic temperature (i.e., 27.6 K), on the other hand, Chaboche 2<sup>nd</sup> order coefficients for Amzirc are taken from the monotonic tensile tests, as already done for electroformed copper. However, as the results derived with these two different approaches (i.e., from monotonic tensile tests or from cyclic mechanical tests) may be incoherent, Chaboche 2<sup>nd</sup> order coefficients using the monotonic tensile tests are obtained in such a way to match the plastic stress differences instead of the absolute values, as graphically represented in Fig. 10 and Fig. 11. Note that such procedure requires the coefficient  $\gamma_1$  at 27.6 K to be imposed a priori.

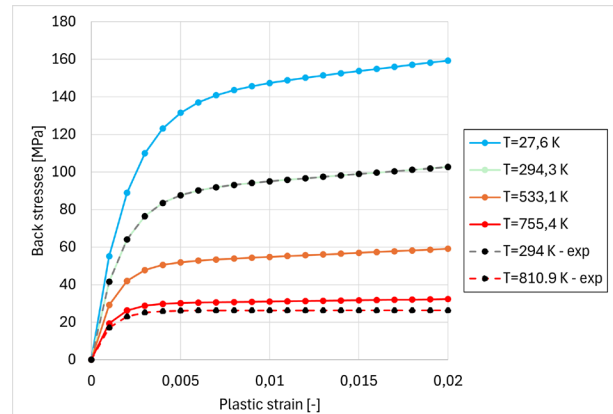


**Fig. 10 – Back stresses – plastic strain Amzirc experimental curves and extrapolated/interpolated curves.**

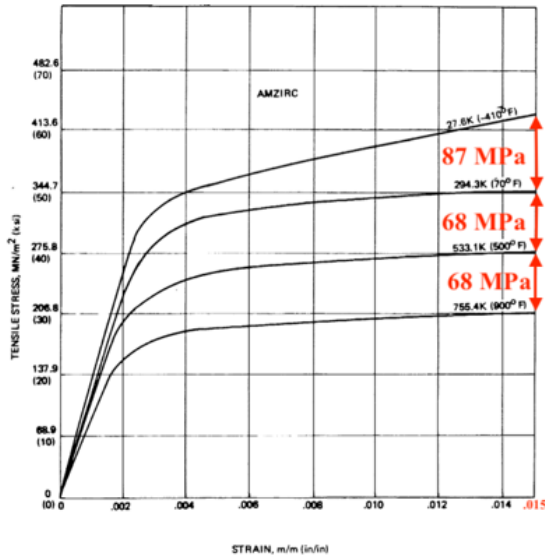


**Fig. 11 – Tensile monotonic stress-strain curves of Amzirc from [2].**

Note also that the Young modulus and the yield strength for the computation of the Amzirc back stresses vs plastic strain curves is computed from the stabilised low cycle fatigue curves available at 294,3 K and 810.9 K and exported or interpolated according to the aforementioned logic. The coefficients found for the Amzirc are given in Table 4.

**Table 4 – 2<sup>nd</sup> order Amzirc Chaboche coefficients.**

Coefficients	27.6 [K]	294.3 [K]	533.1 [K]	755.4 [K]
Amzirc				
C1	27.6	27.4	21.2	15.4
$\gamma_1$	500	624.8	839.2	1038
C2	1.1	0.7	0.4	0.1
$\gamma_2$	0.1	0.1	0.1	0.1

Note that, differently from electroformed copper (Table 3) the R.M.S. error has not been computed since the Amzirc 2<sup>nd</sup> order Chaboche coefficient are computed from interpolated data.

#### 4. Results

The results from the transient thermal analysis at the steady state condition are shown in Fig. 12. The thermal field shows the highest temperature point located at Point A with a value of 797 K. This location corresponds to the mid channel section at the hot-gas side and, consequently, it is the strongest thermally loaded point in the structure.

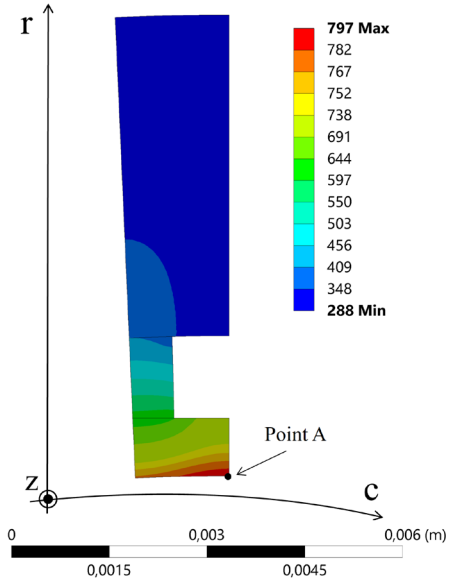


**Fig. 12 – Hot fire phase thermal map.**

The typical channel deformation is presented in Fig. 13 for the initial geometry, for the 1<sup>st</sup> cycle, 20<sup>th</sup> cycle, and 40<sup>th</sup> cycle. Deformations at the steady-state firing phase and at the post cooling phase are represented for the aforementioned cycles.

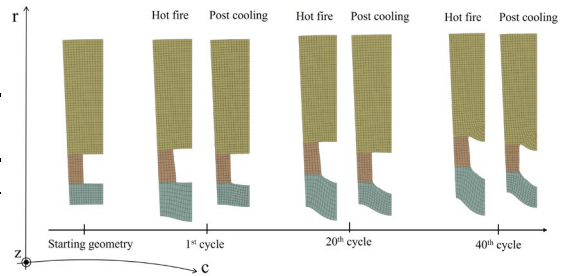


**Fig. 13 – Channel deformation over cycles magnified 24 times for the 2<sup>nd</sup> order Chaboche model.**

Since Point A is the highest temperature point in the structure, the hoop stresses ( $\sigma_{hoop}$ ) and the total hoop strain ( $\epsilon_{tot\_hoop}$ ) at point A, according to the cylindrical coordinate system presented Fig. 5, are represented for every cycle in Fig. 14, Fig. 15, and Fig. 16 for 2<sup>nd</sup> order Chaboche, kinematic and isotropic hardening models, respectively. The progressions of cycles over the time are represented by the black arrows.

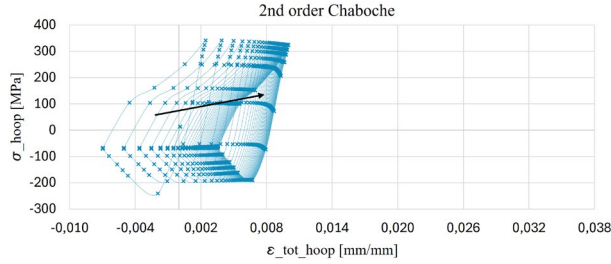


**Fig. 14 – Hysteresis curve of Point A over time for Chaboche model.**

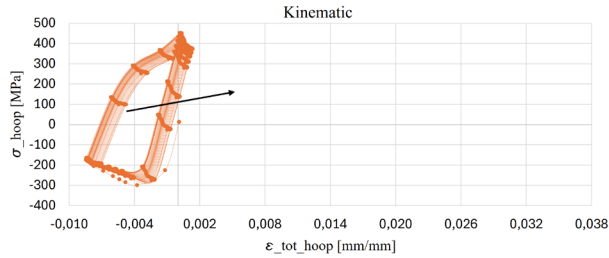


**Fig. 15 – Hysteresis curve of Point A over time for kinematic model.**

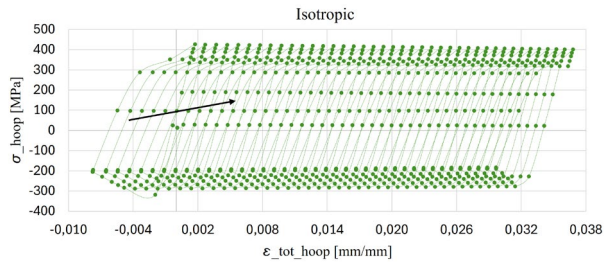


**Fig. 16 – Hysteresis curve of Point A over time for isotropic model.**

Fig. 17 presents the accumulated equivalent hoop plastic strain over time for mentioned hardening models at Point A.

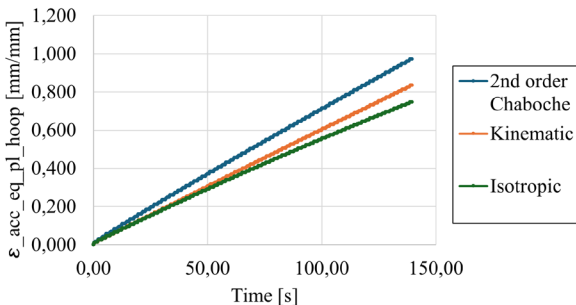


**Fig. 17 – Accumulated equivalent hoop plastic strain over time at Point A.**

## 5. Discussion

The deformations of the structure over cycles (Fig. 13) shows the typical behaviour of a liquid rocket engine inner wall. It consists, during the firing phase, of the expansion of the inner wall due to the maximum temperatures reached at that location, and the stiffening of the outer wall, which is the coldest part of the structure. During the post cooling phase, since the material is plasticised, the inner wall is not able to recovery its original shape. After multiple cycles it results in a thinner inner wall with respect to the original geometry.

The second cycle, for all three hardening models, present the highest difference in terms of  $\Delta\sigma_{hoop}$  and  $\Delta\varepsilon_{tot\_hoop}$  with respect to the first cycle because of the ambient temperature starting point. Comparing the models, the highest difference in terms of  $\Delta\varepsilon_{tot\_hoop}$  between the first and the second cycle is attributed to the Chaboche and the isotropic models. Both models tend to decrease the  $\Delta\varepsilon_{tot\_hoop}$  for single cycle together with the decreasing of  $\Delta\sigma_{hoop}$  for single cycle (Fig. 18). The kinematic model, on the other hand, behaves differently. In particular, while it exhibits a trend similar to that seen with previous models in the few preliminary cycles, later it implies an increasing  $\Delta\sigma_{hoop}$  at almost constant  $\Delta\varepsilon_{tot\_hoop}$ . Hysteresis loops go towards increasing tensile plastic strains (Fig. 14, Fig. 15, Fig. 16) because of the accumulation of plastic strains over cycles (Fig. 17).

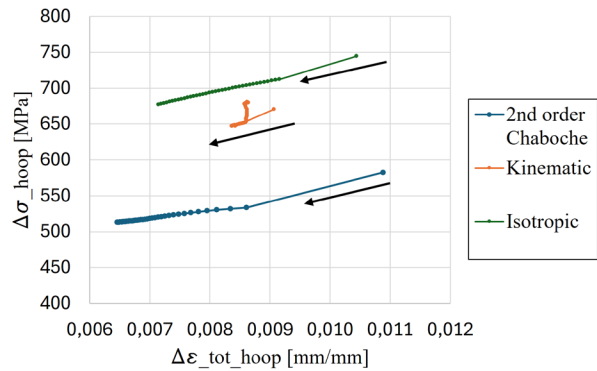


**Fig. 18 – Comparison of stress and strain range par cycle for different hardening models at Point A.**

Since the Chaboche and kinematic models are able to correctly take into account the Bauschinger effect, a remarkable difference in the  $\Delta\sigma_{hoop}$  for single cycle between models is showed (Fig. 18). The isotropic model has the highest  $\Delta\sigma_{hoop}$  compared to Chaboche and kinematic hardening. However, this is not reflected by the  $\Delta\varepsilon_{tot\_hoop}$ , where the highest value is showed by the Chaboche model.

Even though having the highest maximum and minimum stresses, the isotropic and the kinematic models tends to under predict the minimum and the maximum strains per cycle (Fig. 18). Since the failure mechanism is driven by strains, and not stresses, the 2<sup>nd</sup> order Chaboche model results in a safer evaluation of the throat section life behaviour.

The circumferential total strain over the time for point A is compared for the three hardening models (Fig. 19). The isotropic model shows a linear trend over the cycle. Contrary, the 2<sup>nd</sup> order Chaboche behaviour shows a preliminary increase of the  $\epsilon_{tot\_hoop}$  per cycle, but after approximately 12 cycles (42 s) it stabilises.

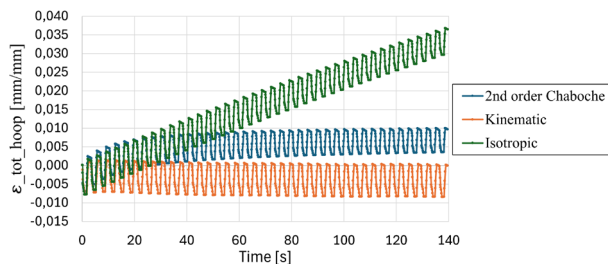


**Fig. 19 – Circumferential total strain at Point A vs time.**

## 6. Conclusions

A sub scale SSME thrust chamber throat section for the LeRC life estimation program has been used as a reference case study for comparing different hardening models by means of finite element thermo-mechanical analysis. The analysis has been focused on the throat section, being the most thermos-mechanically solicited one.

A transient temperature analysis has been carried out to reproduce the temperature distribution experimentally measured during hot fire tests of the plug-chamber SN40, that is composed of a SN40 Amzirc inner wall and electroformed copper closeout. The transient wall temperature behaviour of the cycle, which is practically constant in each cycle, is used as thermal input for the multiple cycles mechanical analysis. The input consists also of the pressure loads generated by the hot-gas and coolant flow. A total of 40 cycles have been simulated.

The results confirm the relatively high deformation of the inner wall together with the conventional hysteresis behaviour of this particular hardware.

Isotropic and kinematic hardening models have been calibrated using monotonic tensile curves at different temperatures for both materials, while 2<sup>nd</sup> order Chaboche model has been calibrated by means of monotonic tensile curves at different temperatures for electroformed copper and by means of single total strain low cycle fatigue tests at different temperatures.

Results show high discrepancy between the hardening models in predicting the mechanical behaviour of the location where maximum thermos-mechanical load occurs, that is the middle point of the channels at the hot gas side.

## References

- [1] R. Quentmeyer, Experimental Fatigue Life Investigation of Cylindrical Thrust Chambers, AIAA/SAE 13th propulsion conference , Orlando, Florida, 1977
- [2] J. Esposito, Thrust chamber life prediction - Volume 1 Mechanical and physical properties of high performance rocket nozzle materials, NASA report CR - 134806, Seattle, Washington, 1975
- [3] J. R. Riccius, Optimization of geometric parameters of cryogenic, 37th AIAA/ASME/SAE/ASEE Joint Propulsion, Salt Lake City, Utah, 2001
- [4] M. Rezaiee-Pajand and S. Sinaie, On the calibration of the Chaboche hardening model and a modified hardening rule for uniaxial ratcheting prediction, International Journal of Solids and Structures Volume 46, Issue 16, 1 August 2009
- [5] J. S. Novak, Parameter estimation of cyclic plasticity models and strain-based fatigue curves in numerical analysis of mechanical components under thermal loads, Master thesis, University of Unide, 2016